

Ultrafast Adaptive Primary Frequency Tuning and Secondary Frequency Identification for S/S WPT system

Chang Liu, *Student Member, IEEE*, Wei Han, *Member, IEEE*, Guangyu Yan, *Student Member, IEEE*, Bowang Zhang, *Student Member, IEEE* and Chunlin Li

Abstract—Magnetic resonance wireless power transfer (WPT) technology is increasingly being adopted across diverse applications. However, its effectiveness can be significantly compromised by parameter shifts within the resonance network, owing to its high system quality factor. Such shifts are inherent and challenging to mitigate during the manufacturing process. In response, this article introduces a rapid frequency tuning approach. Leveraging switch-controlled capacitors (SCC) to adjust the resonance network and the primary side's operating frequency, alongside a current zero-crossing detection (ZCD) circuit for voltage-current phase determination, this method circumvents the need for intricate knowledge of WPT system parameters. Moreover, it obviates the necessity for inter-side communication for real-time identification of the secondary side resonance frequency. The swift response of SCC and two-step perturb-and-observe algorithm mitigate output disturbances, thereby expediting the frequency tuning process. Experimental validation on a 200W Series-Series compensated WPT (SS-WPT) system demonstrates that the proposed method achieves frequency recognition accuracy within 0.7kHz in less than 1ms, increasing system efficiency up to 9%.

Index Terms—frequency tuning, detuning tolerance, parameter identification, wireless power transfer (WPT).

I. INTRODUCTION

WIRELESS power transfer (WPT), powering devices in a cordless way, exhibits the characteristics of higher safety, reliability and convenience. It has been increasingly used in electric vehicles [1], portable consumer electronics [2], medical implants, home appliances and other industrial applications [3], [4], [5]. The high efficiency of WPT systems stems from the elevated quality factor of the resonant network, which, post-bilateral resonance, effectively mitigates reactive power while augmenting transmission power [6]. However, deviations from ideal resonance parameters inevitably lead to decreased system efficiency and output power. In practical scenarios, detuning arises due to several factors. Firstly, inherent inaccuracies in commercial capacitors coupled with discrete capacitance values preclude precise tuning, thereby exacerbating system costs if improved accuracy is pursued. Secondly, ambient temperature variations and aging contribute to capacitance parameter shifts, thereby altering system

resonant frequencies during operation [7], [8], [9]. Thirdly, the mobile nature of receiving ends in WPT systems, compounded by magnetic material effects like ferrite, induces changes in coil self-inductance [10], exacerbating system detuning. Finally, prevalent wireless charging standards like Qi for electronic devices (110kHz~205kHz) or SAEJ2954 for electric vehicles (79kHz~90kHz) mandate a broad resonant frequency range. Consequently, receivers operating within this specified range are deemed compliant, necessitating transmitters to adapt to varying receiver resonant frequencies to enhance overall compatibility. Therefore, researching how to address the frequency mismatch issue in WPT systems is of paramount importance.

The existing methods to solve frequency mismatch in WPT systems can be divided into three categories, which are briefly introduced below.

- 1) Primary frequency tuning: By monitoring the frequency at which the inverter output voltage and current align, known as the Zero Phase Angle (ZPA) point [11], [12], [13], the system can maintain high efficiency even when resonance parameters shift. However, the methods for acquiring phase information and controlling frequency differ. Likewise, in [9], Bosshard et al. employed the zero-crossing detection (ZCD) signal of the primary current to modulate the frequency, ensuring zero voltage switching (ZVS) of the IGBT across a broad load spectrum. Meanwhile, Sun et al. in [14] utilized the ZCD signal of the primary current to adjust the frequency waveform, ensuring operation at the optimal ZVS frequency rather than a distorted ZVS frequency. When the parameters of the secondary resonant network are misaligned, this approach fails to maintain the natural resonant frequency of the secondary side in sync with the operating frequency. Consequently, incomplete tuning of the WPT system occurs, leading to a subsequent decrease in efficiency.
- 2) Secondary frequency tuning: This is normally achieved by introducing various reactive power compensation devices on the secondary side. When the system's operating frequency aligns with the inherent resonance frequency of the primary side, excess reactive power is compensated for. In [15], this is accomplished by a gyrator constructed by DAB; in [16], by the SSC; and in [17], by the variable

reactor. Additionally, to minimize the need for extra reactive power devices, Dai et al. and Rong et al. achieved similar effects using a single-phase active rectifier bridge [18], [19]. Nevertheless, these solutions inevitably lead to increased manufacturing costs, larger physical volumes, and heightened control complexities on the secondary side. In applications such as wireless charging for electric vehicles, simplicity and lightweight design are paramount considerations for the receiving end.

- 3) Double-side frequency tuning: Due to the inevitable deviations in capacitance and coil parameters on both primary and secondary sides, stabilizing the inherent resonance frequency discrepancy can be achieved by introducing variable capacitance while maintaining a fixed operating frequency. For instance, in [20], Han et al. utilized a unique switchable capacitor structure to counteract efficiency degradation caused by variations in secondary-side inductance. However, this approach is not feasible as the undetectable induced voltage on the secondary side is utilized for circuit control. Recently, Tan et al. achieved bidirectional tuning through the deployment of SCCs on both sides [21]. They utilized the primary-side SCC to track the ZPA point and the secondary-side SCC to track the maximum output current, thus achieving decoupled control of both sides. The similar hardware configuration is adopted in [10] to compensate for the self-inductance variations of transmitter and receiver. However, it should be noted that this approach comes with higher costs.

In the aforementioned methods, parameter identification techniques are employed in [18] and [10] to estimate the parameters of inductance or compensating capacitance, facilitating frequency tuning. Meanwhile, approaches for identifying parameters of the secondary resonant network are presented in [22], [23], and [24]. In [22], Liu et al. employed hardware-based d/q transformation methods, followed by signal processing to detect deviations in resonant capacitance. However, this method incurs high hardware costs and involves complex algorithms. Yang et al. utilized wide-ranging frequency sweeps and a two-layer ADE algorithm to accurately identify the parameters of the secondary resonant network [23]. Nonetheless, this approach is time-consuming. In [24], the SCC is adjusted to operate the system in a bidirectional tuning state after identifying the resonant frequency of the secondary side. However, during parameter identification, significant frequency variations occur in [23] and [24], which poses challenges for online identification.

Therefore, to equip the WPT system with the ability to swiftly detect secondary-side resonant frequency deviation and promptly restore full resonance, this paper proposes a rapid online identification method for the secondary-side resonance frequency. This method introduces a SCC on the primary side, allowing the system to operate in distinct phases: a rapid identification phase and a ZVS or quasi-ZPA operation phase. Unlike existing methods, the proposed approach doesn't require any secondary-side information throughout the entire process, thus eliminating the need for wireless communication

dependency. Moreover, by simplifying the design of the secondary side, it not only reduces overall manufacturing costs but also enhances the receiver's ability to cope with parameter deviations caused by factors such as manufacturing variations or aging processes. Since the frequency perturbation applied during the identification process is minimal, it does not disrupt normal system output. This solution is particularly suitable for transmitter-side design in static wireless charging for electric vehicles.

The remainder of this article is structured as follows: In Section II, we compare and analyze the characteristics of the SS-WPT system under varying detuning conditions. Subsequently, in Section III, we propose an adaptive fast frequency tuning method. Section IV presents experimental verification, where various conditions are tested for comparison of tuning and identification results. Finally, Section V offers concluding remarks for this article.

II. DETUNING CONDITION ANALYSIS

A. Characteristics of SS-WPT system

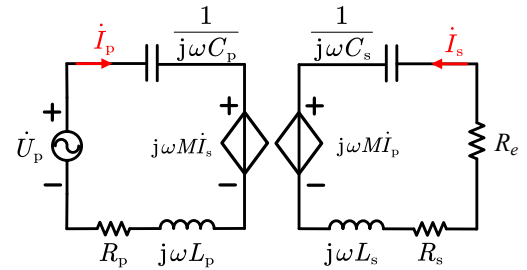


Fig. 1. Circuit model of SS-WPT system.

Due to its simplicity and the fact that its inherent resonance frequency remains unaffected by load and mutual inductance, this paper focuses on the series-series (SS) topology as an example. As illustrated in Fig. 1., L_p (L_s) and R_p (R_s) represent primary (secondary) self-inductance and parasitic resistance. C_p and C_s are the corresponding compensation capacitors. R_e represents the equivalent load resistance. Therefore, the inherent resonant angular frequencies of the primary and secondary sides are given by:

$$\omega_p = 1/\sqrt{L_p C_p} \quad (1)$$

$$\omega_s = 1/\sqrt{L_s C_s} \quad (2)$$

The system's characteristics can be described according to Kirchhoff's Voltage Law (KVL) after implementing first harmonic analysis (FHA) as (3), where \dot{U}_p , \dot{I}_p , \dot{I}_s are the phasors of fundamental input ac voltage and current of primary and secondary coils. X_p and X_s refer to the reactance of resonators on both sides as indicated in (4).

$$\begin{bmatrix} \dot{U}_p \\ 0 \end{bmatrix} = \begin{bmatrix} R_p + jX_p & j\omega M \\ j\omega M & R_s + R_e + jX_s \end{bmatrix} \begin{bmatrix} \dot{I}_p \\ \dot{I}_s \end{bmatrix} \quad (3)$$

$$\begin{cases} X_p = \omega L_p - 1/(\omega C_p) \\ X_s = \omega L_s - 1/(\omega C_s) \end{cases} \quad (4)$$

Therefore, ac-ac transmission efficiency, the input

impedance and power factor of SS-WPT system can be obtained by (5), (6) and (7) respectively.

$$\eta = \frac{I_s^2 R_L}{I_p^2 R_p + I_s^2 (R_s + R_L)} \quad (5)$$

$$= \frac{\omega^2 M^2 R_L}{[(R_s + R_L)^2 + X_s^2] R_p + \omega^2 M^2 (R_s + R_L)}$$

From (5), it can be observed that, with other parameters held constant, the system efficiency is maximized when X_s is zero. Furthermore, the system transfer efficiency is independent of the magnitude of X_p .

Moreover, from (6) and (7), it can be deduced that when X_s is zero, setting X_p to zero as well can increase the power factor. Therefore, for SS-WPT systems under fixed load and mutual inductance conditions, adjusting both sides' reactance to zero can optimize system efficiency and minimize reactive power.

$$Z_{in} = \left(R_p + \frac{\omega^2 M^2 (R_s + R_e)}{(R_s + R_e)^2 + X_s^2} \right) \quad (6)$$

$$+ j \left(X_p - \frac{\omega^2 M^2 X_s}{(R_s + R_e)^2 + X_s^2} \right)$$

$$PF = \frac{\text{Re}[Z_{in}]}{|Z_{in}|} \quad (7)$$

However, variations in self-inductance due to changes in coil relative positioning [10] or incomplete compensation caused by manufacturing errors and aging processes in capacitors may lead to deviations in the inherent resonance frequency of the secondary side. Consequently, the system may fail to achieve optimal efficiency. To simplify the analysis, in this section, we assume that the coil's self-inductance remains constant, and the variation in the inherent resonance frequency of the secondary side is achieved by adjusting the corresponding compensation capacitance. Because changing the resonance frequency of the secondary side by varying the self-inductance with coil relative positioning is difficult to achieve experimentally. For ease of presentation, the system parameters are as shown in Table I for the subsequent calculations.

TABLE I
PARAMETERS FOR THEORETICAL CALCULATIONS

| Items | Symbol | Value |
|--------------------------------|----------|---------------|
| Input voltage RMS | U_p | 40 V |
| Primary-side Capacitor | C_p | 29.46 nF |
| Secondary-side Capacitor | C_{s0} | 38.01 nF |
| ESR of transmitter | R_p | 0.3 Ω |
| Self-inductance of transmitter | L_p | 119 μ H |
| ESR of receiver | R_s | 0.3 Ω |
| Self-inductance of receiver | L_s | 92.23 μ H |
| Coupling coefficient | k | 0.1~0.2 |
| Equivalent load resistance | R_e | 2~20 Ω |
| Detuning range | Δ | -0.2~0.2 |

B. Efficiency and power factor of detuned system

To ensure compliance with the SAEJ2954 standard, the value of C_s is designed to resonate with L_s at 85 kHz, denoted as C_{s0} . The deviation caused by various factors is represented by ΔC_{s0} . Substituting the value of C_s from equation (8) into equation (5), the variation of system efficiency with the secondary-side

detuning state is obtained. Similarly, by simultaneously combining equations (4), (6), (7) and (8), the relationship between the power factor and the variation of detuning state can be derived, as shown in Fig. 2.

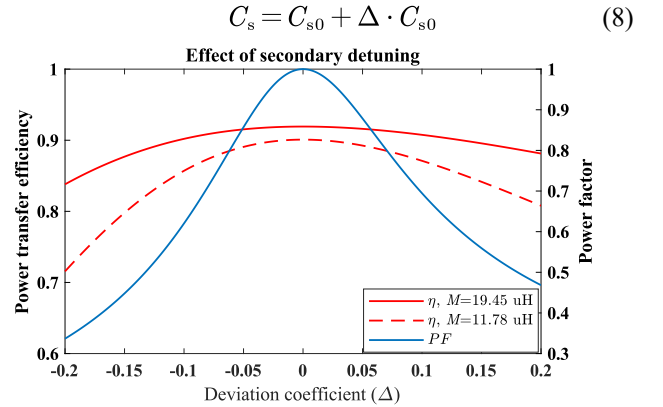


Fig. 2. Effect of secondary detuning on system efficiency and power factor.

The coupling coefficient of two coils are:

$$k = \frac{M}{\sqrt{L_p L_s}} \quad (9)$$

As is demonstrated in Fig. 2, the efficiency and power factor deviation are more obvious under weaker coupling conditions.

C. Comparison of different frequency tuning methods

The relationship between system transfer efficiency and detuning level under different control methods is illustrated in Fig. 3.

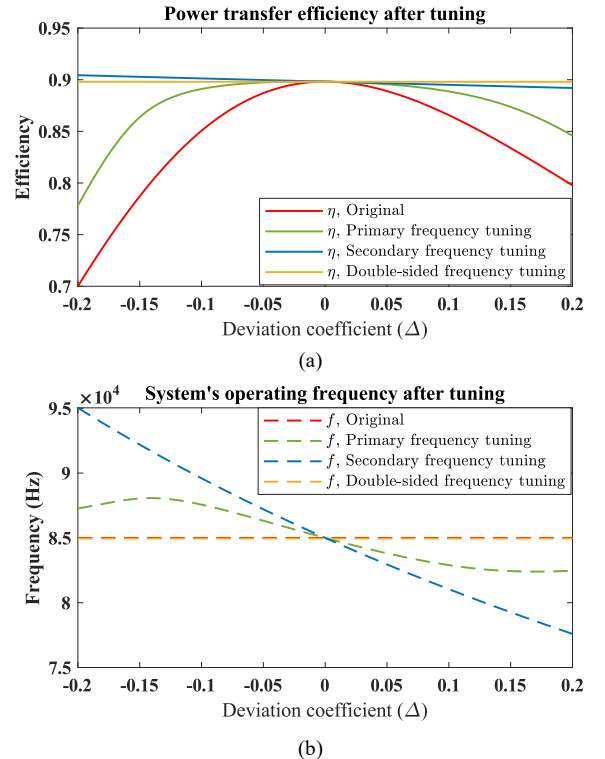


Fig. 3. Effect of different tuning methods on system efficiency with variation of secondary inherent frequency. (a) System efficiency after tuning. (b) Operating frequency after tuning.

- 1) Primary frequency tuning: This method achieves partial compensation for secondary-side detuning by altering the inverter output frequency to track the ZPA point of the input impedance [11], [13], [25], [26]. As previously discussed, the system achieves maximum efficiency when the operating frequency matches the inherent resonance frequency of the secondary side. Therefore, as depicted by the green line in Fig. 3, this method tracks the ZPA frequency within a certain frequency range, which closely matches the secondary-side resonance frequency, thus improving efficiency. The main advantage of this method is that it does not require additional power devices, and its implementation is simple. However, the range of efficiency improvement is limited.
- 2) Secondary frequency tuning: This method can maintain relatively high system efficiency over a wide range of detuning levels by tracking the inherent resonance frequency of the secondary side, as shown by the blue curve in Fig. 3. However, the challenge lies in determining this inherent resonance frequency. Additionally, when the operating frequency is adjusted to match the secondary-side resonance frequency, it may increase the reactive power of the primary-side resonant system, thereby lowering the power factor of the system.
- 3) Double-side frequency tuning: For this method, fixed frequency control can be utilized with compensation applied separately to the primary and secondary sides. However, this approach imposes additional requirements on the secondary side, increasing control complexity. For instance, it may necessitate the introduction of variable capacitor [20], [21], [22] or semi-active rectification [27] on secondary side, or it may require additional wireless communication [20]. Therefore, while this method theoretically ensures high efficiency over a wide detuning range, it reduces the adaptability of the transmitter to different receivers and increases the cost of the receiver.

Therefore, the identification of the inherent resonance frequency of the secondary side is crucial for improving system efficiency. The method proposed in this paper achieves high efficiency and high power factor by identifying and controlling the operating frequency to match the secondary-side resonance frequency, while introducing variable capacitance on the primary side. This approach allows for efficient operation at the specified frequency range while achieving fault diagnosis beyond this range.

III. ULTRAFast FREQUENCY TUNING

A. Identification of secondary resonant frequency

The following derivations of secondary resonant frequency are based on three assumptions.

- 1) The influence of parasitic resistances R_p and R_s are neglected, since in normal operation range they are relatively much smaller than R_e or reflected impedance.
- 2) Primary side reactance X_p is assumed to be 0 under different working frequencies. This is achieved by

adjusting the control angle of SCC as depicted in Fig. 4.

Given the short duration and small magnitude of the frequency disturbance, it is assumed that the equivalent load resistance R_e remains constant.

Based on the above assumptions, according to (6) the angle θ of Z_{in} can be expressed as:

$$\tan \theta = \frac{1/(\omega C_s) - \omega L_s}{R_e} \quad (10)$$

If two known angular frequencies ω_m and ω_n are given, and the input impedance angles corresponding to these states are measured, the ratio of the tangents of the two impedance angles can be obtained and defined as k_{mn} in (11).

$$\frac{\tan \theta_m}{\tan \theta_n} = \frac{1/(\omega_m C_s) - \omega_m L_s}{1/(\omega_n C_s) - \omega_n L_s} \triangleq k_{mn} \quad (11)$$

Transforming the above equation, we can obtain:

$$L_s C_s = \frac{(\omega_n - k_{mn} \omega_m)}{\omega_m \omega_n (\omega_m - k_{mn} \omega_n)} \quad (12)$$

By combining equations (2) and (12), the inherent resonance angular frequency of the secondary side can be obtained as:

$$\omega_s = \sqrt{\frac{\omega_m \omega_n (\omega_m - k_{mn} \omega_n)}{(\omega_n - k_{mn} \omega_m)}} \quad (13)$$

From the above derivation, it can be seen that this method only requires the introduction of phase detection functionality to rapidly obtain the inherent resonance frequency of the secondary side. It does not necessitate any parameters of the secondary side components, mutual inductance, or wireless communication.

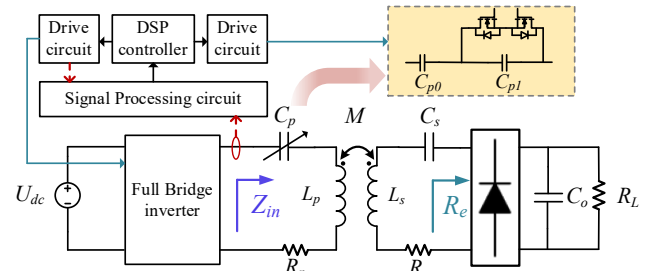


Fig. 4. System structure of SS-WPT with secondary resonant frequency identification capability.

B. Error Analysis

Due to the normal operating frequency specified by the SAE J2954 standard being 85kHz, it can be considered that designing the secondary side to resonate at this frequency is the target. Therefore, the initial selection of two operating frequencies for identification can be designated as 84kHz and 86kHz. This choice of frequencies minimizes the impact on the system output from frequency disturbances while ensuring that phase differences remain distinguishable. As shown in Fig. 5 and Fig. 6, the horizontal axis represents the inherent resonance frequency f_s of the secondary side, and f_{ref} indicates the reference line where the identification frequency equals f_s . The orange line f_{ido} represents the identification result without any disturbances. It can be observed that f_{ido} closely matches f_{ref} , demonstrating that, under the assumptions described earlier,

this method can achieve high-precision identification with different f_m and f_n .

However, during the actual identification process, there may be factors leading to frequency offset during identification, which include:

- 1) Load disturbance: Due to frequency changes, the equivalent load resistance will be subjected to a certain degree of disturbance, as shown by f_{id1} curve in Fig. 5.
- 2) Incomplete compensation of primary side inductance by SCC: Due to factors such as control precision, the size of the equivalent capacitance of SCC deviates from the ideal capacitance value corresponding to complete compensation of inductance. This is illustrated by f_{id2} curve in Fig. 5, whose magnitude of disturbance is about 2% tolerance in the equivalent capacitance of the SCC.
- 3) Phase measurement error: This error directly affects the parameter k_{mn} in (11), thereby influencing the result of the identification frequency, as illustrated by f_{id3} in Fig. 5. It represents an error of approximately 200 ns during phase measurement.

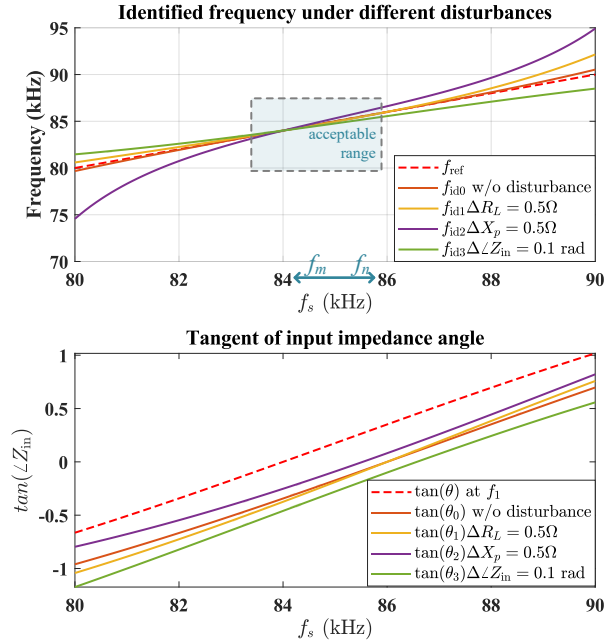


Fig. 5. Identified frequency and input impedance angle with variation of secondary resonant frequency under different types of disturbance with $f_m = 84\text{kHz}$, $f_n = 86\text{kHz}$.

From the results of the identification frequency in Fig. 5, it is evident that within the range of 84 to 86 kHz, the maximum identification error is approximately 0.5 kHz, which is generally acceptable. However, below 82 kHz and above 88 kHz, the influence of disturbances is quite evident, with errors exceeding 5 kHz. By observing the differences in the input impedance angle under different disturbances compared to the undisturbed condition in Fig. 5, it can be seen that besides the phase measurement error, which is independent of frequency, the impedance angle error caused by load disturbances and incomplete compensation is closer to the undisturbed condition between 84 and 86 kHz. Therefore, it is possible to improve the

identification accuracy by adjusting the frequency used for identification.

As shown in Fig. 6(a), by changing the identification frequency f_m to 86kHz and f_n to 88kHz, the identification accuracy between 86 and 90kHz can be improved. At this time, the maximum load disturbance caused is only 0.3kHz, and the error caused by other factors is also limited to 1.5kHz; similarly, in order to improve the identification accuracy in the 80 to 84kHz frequency band, the detection frequency is adjusted to 84kHz and 82kHz, and the maximum identification error is reduced from 5.4kHz to 0.8kHz, as presented in Fig. 6(b).

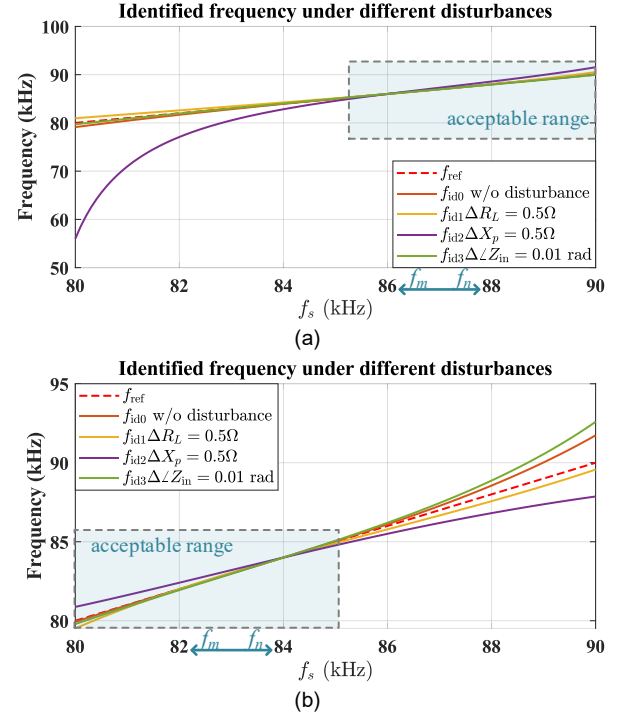


Fig. 6. Identified frequency with variation of secondary resonant frequency under different types of disturbance with (a) $f_m = 86\text{kHz}$, $f_n = 88\text{kHz}$, (b) $f_m = 84\text{kHz}$, $f_n = 82\text{kHz}$.

Based on the analysis above, this paper proposes a two-step perturb-and-observe method. Initially, identification is performed using frequencies of 84 kHz and 86 kHz. If the identified frequency range in this step is greater than 86 kHz, then 86 kHz and 88 kHz are used for a second identification. Conversely, if the identified range is below 84 kHz, then 84 kHz and 82 kHz are used for a second identification. This approach enables the rapid and accurate identification of the inherent resonance frequency of the secondary side within the frequency range of 79 kHz to 90 kHz specified by the SAE J2954 standard.

C. System Configuration and Control Strategy

Fig. 7 illustrates system configuration and control scheme of SS-WPT with ultrafast secondary resonant frequency identification capability. The full-bridge inverter provides high-frequency ac power input, while the SCC is used to adjust the capacitance on the primary side. The phase detection of voltage and current is achieved by utilizing the ZCD signal of the current required by the SCC itself and the drive signal of the

inverter. By feeding these two signals into a D flip-flop, the lead-lag relationship between voltage and current can be ascertained. When input them into an XOR gate, the absolute value of the phase difference can be determined.

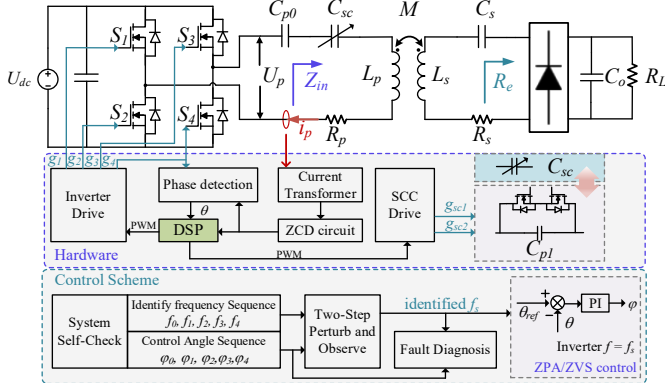


Fig. 7. System configuration and control scheme of SS-WPT with ultrafast secondary resonant frequency identification capability.

The system operates according to the following workflow:

- 1) System self-check: When the secondary side is not connected, the input voltage is reduced, and the input current is limited. The inverter frequency is adjusted according to the given frequency sequence for identification, and the SCC control angle sequence for achieving phase alignment of primary side voltage and current is obtained through PI control. In this case, if the obtained control angle sequence cannot achieve the control objective of phase alignment between voltage and current, it is considered that there is a significant deviation in the primary side capacitance, which requires replacement. The fault is reported accordingly.
- 2) Two-step perturb-and-observe: Run the identification algorithm to determine the inherent resonance frequency of the secondary side. Details of the algorithm are presented in Fig. 7.
- 3) ZPA/ZVS control: To improve the power factor of the primary side operating at f_s , PI control is applied to the SCC to ensure that the inverter operates in the ZPA or ZVS state. This increases the power factor on the primary side and ensures efficient operation of the system.

Fig. 8 illustrates the control flowchart of the system, annotating the various frequencies used. Initially, the system assumes the inherent resonance frequency of the secondary side as f_0 . When the input impedance angle exceeds a reference value, indicating detuning of the secondary side, frequency identification is required. The identification process is divided into two steps: firstly, perturbation observation is conducted using f_1 and f_2 to obtain an estimated f_s value. Subsequently, based on this estimate and the magnitudes of f_1 and f_2 , a new set of perturbation frequencies is selected for another round of observation, resulting in the final identified f_s value. If this frequency falls within the range specified by the SAE J2954 standard, i.e., from 79 kHz to 90 kHz, then adjust the inverter frequency to this frequency. Otherwise, if severe detuning of the secondary side is detected, report a fault, and limit the frequency range accordingly.

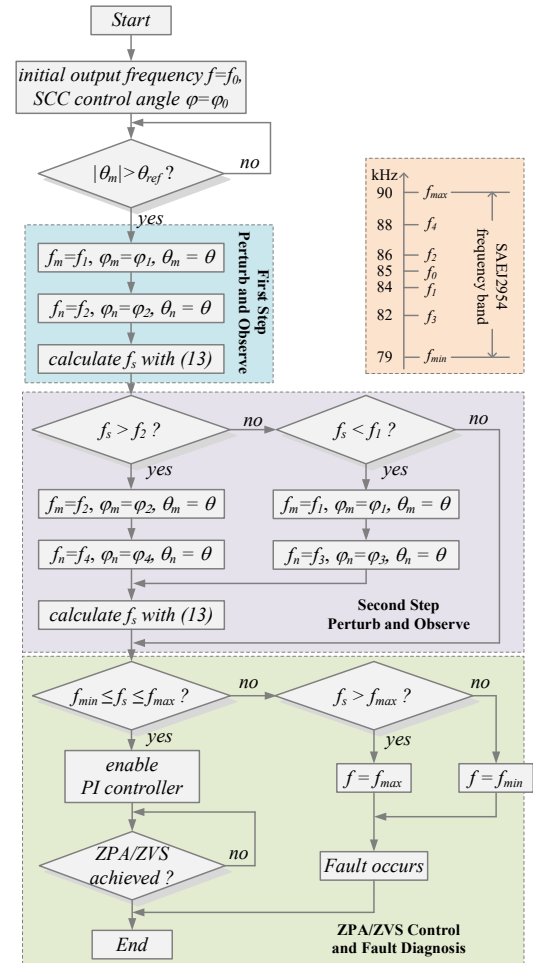


Fig. 8. Flowchart of frequency identification and tuning control strategy.

D. Principal of Switch-Controlled Capacitor

The typical structure and waveforms of SCC are shown in Fig. 9. Assuming a sinusoidal current i_p flowing through the circuit, continuously adjusted capacitor is achieved by varying the duty cycle of the current flowing through the capacitor C_{p1} and its parallel branch (composed of a pair of MOSFETs in a common sourced configuration).

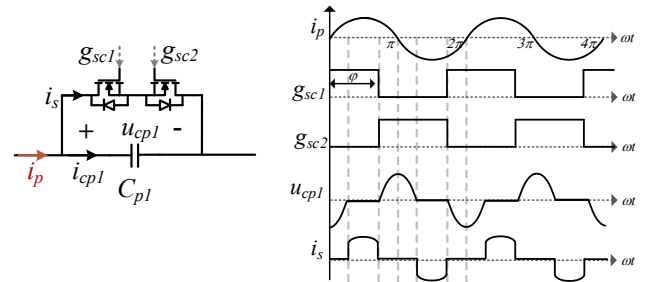


Fig. 9. Typical structure and waveforms of SCC.

By performing Fourier analysis on the voltage waveform across the capacitor terminals u_{cp1} at different control angles, the corresponding equivalent capacitance magnitude C_{sc} under the fundamental frequency can be obtained as [28]:

$$C_{sc} = \frac{\pi C_{p1}}{2\pi - 2\varphi + \sin 2\varphi} \quad (14)$$

Connecting the capacitor C_{p0} in series with C_{sc} not only reduces voltage stress but also mitigates the issue of significant variations in equivalent capacitance when the control angle is large [24]. Therefore, the maximum and minimum values of the primary side capacitance C_p are:

$$\begin{cases} C_{p\min} = \frac{C_{p0} \cdot C_{p1}}{C_{p0} + C_{p1}} \\ C_{p\max} = C_{p0} \end{cases} \quad (15)$$

To ensure that the primary side inductance is compensated at different frequencies, it is necessary to satisfy:

$$[C_{p\min}, C_{p\max}] \supseteq \left[\frac{1}{\omega_{\max}^2 L_p}, \frac{1}{\omega_{\min}^2 L_p} \right] \quad (16)$$

Given the conditions outlined in equations (15) and (16), a smaller value of C_{p0} allows it to bear a larger portion of the voltage across C_p thereby reducing the voltage stress of the SCC.

IV. EXPERIMENTAL VERIFICATION

The feasibility of primary side frequency tuning and secondary side frequency identification for SS-WPT system is demonstrated in this section.

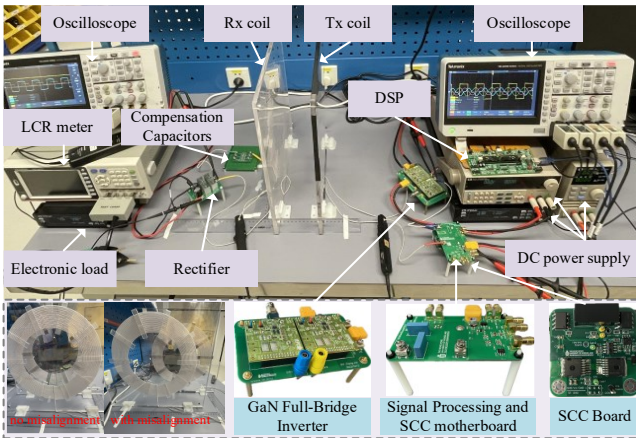


Fig. 10. Experimental setup of SS-WPT with secondary resonant frequency identification capability.

As shown in Fig. 10, a 200 W SS-WPT experimental platform is built. EPC 9099 GaN half-bridge modules are used to form a full-bridge inverter. IMBG65R072M1H CoolSiC MOSFETs from Infineon are used for SCC. TMS320F28335 from TI is applied as digital controller. LCR-8205 from GW Instek is utilized to measure the accurate value of compensation capacitances, self-inductances, and mutual inductance in the system.

To validate the efficacy of the proposed method under various mutual inductance and load conditions, experiments for frequency identification were conducted with and without coil misalignment, as well as under different load scenarios, as depicted in Fig. 10 and summarized in Table II. The load resistance is selected to achieve a relative high efficiency under the constraint that the input current is less than 10A. Moreover, in Table II, system parameters measured under misalignment condition are denoted in parentheses.

TABLE II
PARAMETERS FOR EXPERIMENT VERIFICATION

| Items | Symbol | Value |
|--------------------------|----------|-------------------------|
| DC Bus Voltage | U_{dc} | 40 V |
| Primary-side Capacitor | C_{p0} | 35.21 nF |
| Primary-side Capacitor | C_{p1} | 98.56 nF |
| Secondary-side Capacitor | C_s | 34.97, 40.79 nF |
| ESR of transmitter | R_p | 0.3 Ω |
| Self-inductance of Tx | L_p | 118.27 (118.30) μ H |
| ESR of receiver | R_s | 0.3 Ω |
| Self-inductance of Rx | L_s | 91.95 (91.58) μ H |
| Mutual inductance | M | 19.45 (11.78) μ H |
| Load resistance | R_L | 4, 8 Ω |

A. System Self-Check

Before the secondary side is connected, a smaller input voltage is used to power the LCR circuit of the primary side, and PI control is used to calibrate the SCC control angle at different frequencies so that the output voltage and current of the inverter are in phase, as shown in Fig. 11. There is a slight difference between the SCC control angle obtained by PI control and calculating according to (14). This may be due to factors such as the tolerance of the capacitor itself and the delay of the SCC drive circuit.

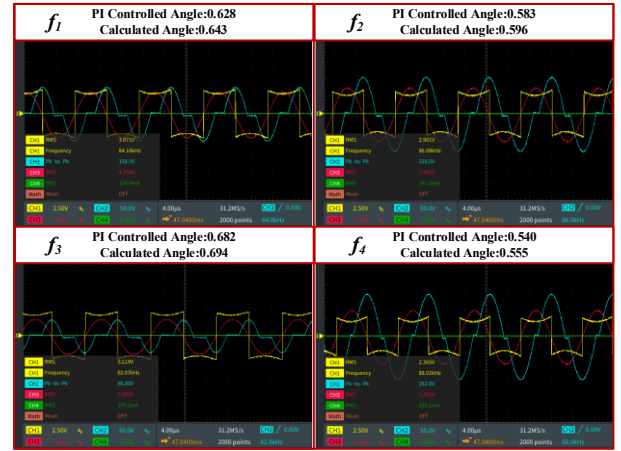


Fig. 11. Experimental waveforms of system self-check.

B. Frequency identification

Table III presents the settings for different cases during the experiment, designed to individually assess the effectiveness of frequency identification across varying frequencies, mutual inductances, and loads.

TABLE III
EXPERIMENT CONDITIONS

| Cases | C_s | f_s (kHz) | Misalignment | R_L | Control |
|-------|-------|-------------|--------------|------------|---------|
| I | 40.79 | 82.178 | Without | 8 Ω | ZPA |
| II | 34.97 | 88.756 | Without | 8 Ω | ZVS |
| III | 34.97 | 88.934 | With | 8 Ω | ZVS |
| IV | 34.97 | 88.934 | With | 4 Ω | ZPA |

Fig. 12 provides the system waveforms before and after frequency tuning when the coils are aligned. In this scenario, Case I and Case II have the same load, but different secondary-side resonant frequencies. The identification errors are 0.382 kHz and -0.196 kHz, respectively. At the same time, ZPA and ZVS control are also realized for each case respectively.

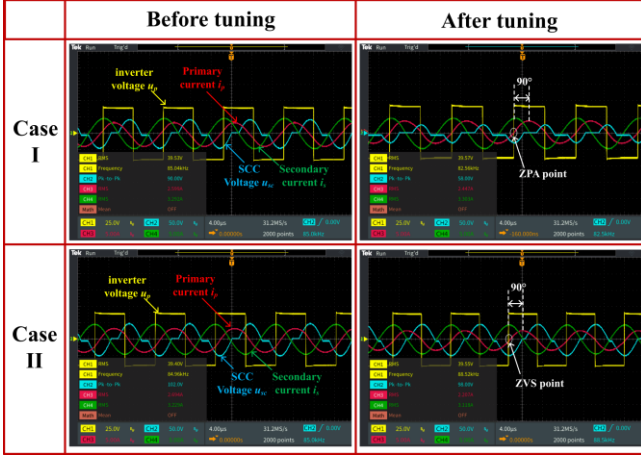


Fig. 12. Experimental waveforms of proposed system before and after tuning process without misalignment.

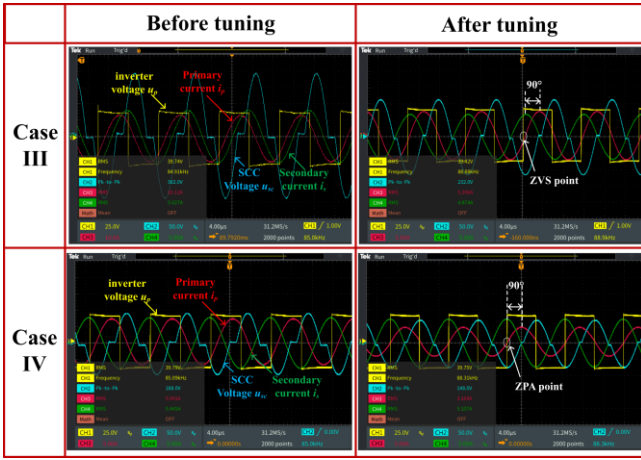


Fig. 13. Experimental waveforms of proposed system before and after tuning process with misalignment.

Similarly, in cases where the coil position and load change, the model can complete the identification of the secondary-side resonant frequency without model parameter adjustment, as shown in Fig. 13 for Case III and Case IV. Additionally, in cases of misalignment, the increased primary-side current stress caused by detuning on the secondary side is very apparent before tuning process in Case III. Therefore, rapid, accurate, and real-time monitoring of the secondary-side resonant frequency is crucial to ensuring the stability of the system. In both Case III and Case IV, ZVS or ZPA were achieved, with the estimated errors being -0.354 kHz and -0.624 kHz, respectively. As evidenced in Fig. 12 and Fig. 13, a 90-degree phase shift between the primary-side voltage and current was observed, validating the accuracy of the frequency identification algorithm

C. Response time

Fig. 14 and Fig. 15 respectively depict the transient changes in the primary and secondary sides of the proposed SS-WPT system before and after frequency tuning. From both figures, it can be observed that the two-step perturb-and-observe algorithm completes identification within 1 ms and rapidly adjusts the output to the secondary side resonance frequency.

Compared to the previously fastest decoupling control-based approach [27], the speed is doubled, and there is no need for complex decoupling transformer design.

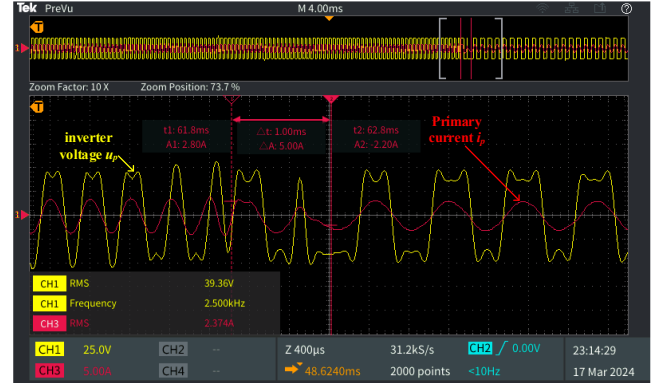


Fig. 14. Transient waveforms of inverter output voltage and current before and after frequency tuning process.

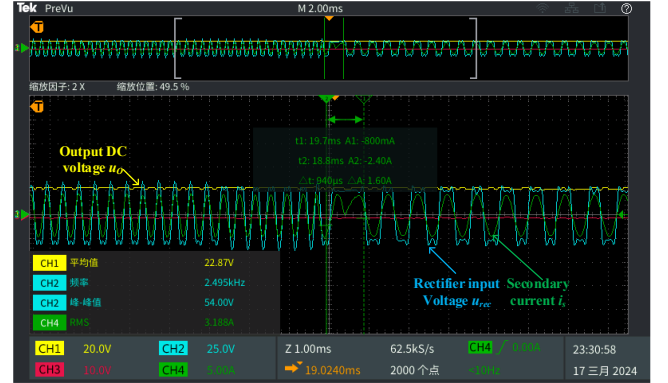


Fig. 15. Transient waveforms of rectifier input voltage and current before and after frequency tuning process.

Furthermore, from Fig. 15, it can be observed that due to the fast identification speed and small perturbation, the disturbance process has minimal impact on the output voltage. This further reduces the influence of load disturbances on the algorithm and improves the accuracy of identification. Compared to previous wide-range frequency sweep parameter identification schemes, this method can be used for online frequency identification, and even dynamic WPT.

D. Efficiency Comparison

As shown in Fig. 16, the changes in DC output power and efficiency (from inverter output to rectifier output) under different cases before and after frequency tuning are illustrated. It can be observed that, in the cases that are without misalignment, where there is relatively high mutual inductance, the improvement in system efficiency through frequency tuning is not significant, approximately 1% to 3%. However, it effectively reduces the input current stress, as seen in Fig. 12, while maintaining a relatively stable output power. In the cases that are misaligned, where there is relatively low mutual inductance, the system's efficiency is improved by 9% after frequency tuning. Additionally, it enhances the power factor on the input side, as shown in Fig. 13. Since this study focuses on the frequency range specified by the SAEJ2954 standard for

identification and experimentation, the frequency deviation range is not too large. In practical applications, the aging and faults of resonant capacitors may significantly mitigate the system performance.

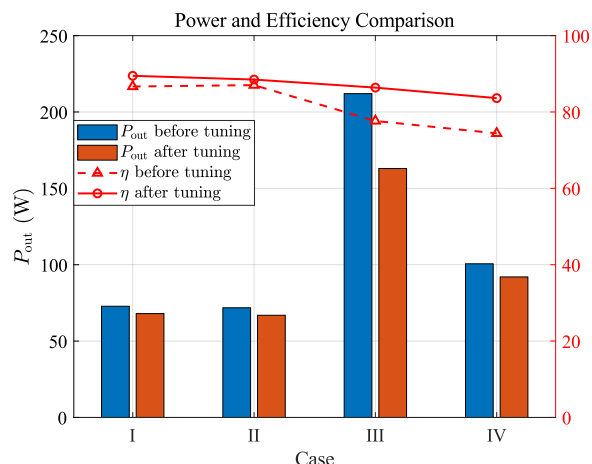


Fig. 16. Output power and system efficiency of different experimental cases before and after tuning process.

V. CONCLUSION

The proposed method in this paper addresses the inherent frequency identification of the secondary side and dynamic compensation of the primary side reactance in SS-WPT systems. The method is analyzed under various disturbances, and a two-step perturb-and-observe algorithm is introduced to enhance the robustness of identification. Without requiring the parameters of the original primary and secondary sides or wireless communication, the method achieves frequency identification within 1 ms with an accuracy of within ± 0.7 kHz. The tuning time is reduced by 50% compared to the existing method. This method can enhance the adaptability of the transmitter end of SS-WPT systems to different receivers compliant with the SAEJ2954 standard and detect significant system detuning faults. In the future, further research will explore how this method can be applied to different WPT topologies.

REFERENCES

- [1] D. Patil, M. K. McDonough, J. M. Miller, B. Fahimi, and P. T. Balsara, "Wireless Power Transfer for Vehicular Applications: Overview and Challenges," *IEEE Trans. Transp. Electrification*, vol. 4, no. 1, pp. 3–37, Mar. 2018, doi: 10.1109/TTE.2017.2780627.
- [2] "Qi wireless charging," *Wireless Power Consortium*. [Online]. Available: <https://www.wirelesspowerconsortium.com/standards/qi-wireless-charging/>. [Accessed: 21-Mar-2024].
- [3] W. Han, K. T. Chau, W. Liu, X. Tian, and H. Wang, "A Dual-Resonant Topology-Reconfigurable Inverter for All-Metal Induction Heating," *IEEE J. Emerg. Sel. Top. Power Electron.*, pp. 1–1, 2021, doi: 10.1109/JESTPE.2021.3071700.
- [4] W. Liu, K. T. Chau, C. H. T. Lee, L. Cao, and W. Han, "Wireless Power and Drive Transfer for Piping Network," *IEEE Trans. Ind. Electron.*, vol. 69, no. 3, pp. 2345–2356, Mar. 2022, doi: 10.1109/TIE.2021.3068675.
- [5] W. Han, K. T. Chau, L. Cao, Z. Hua, and T. Yang, "S-CLC Compensated Wireless Power Transfer With Pulse-Frequency-Modulation Control for Dimmable Low-Pressure Sodium Lamps," *IEEE Trans. Magn.*, vol. 57, no. 2, pp. 1–7, Feb. 2021, doi: 10.1109/TMAG.2020.3026681.
- [6] A. P. Sample, D. T. Meyer, and J. R. Smith, "Analysis, Experimental Results, and Range Adaptation of Magnetically Coupled Resonators for Wireless Power Transfer," *IEEE Trans. Ind. Electron.*, vol. 58, no. 2, pp. 544–554, Feb. 2011, doi: 10.1109/TIE.2010.2046002.
- [7] *Film Capacitors—General Technical Information*. Tokyo, Japan: TDK, 2018. Accessed: Mar. 21, 2024. [Online]. Available: <https://www.tdk-electronics.tdk.com/download/530754/480aeb04c789e45ef5bb9681513474ba/pdf-generaltechnicalinformation.pdf>
- [8] *Ceramic Capacitor Aging Made Simple*. Camarillo, CA, USA: Johanson Dielectrics Inc, 2021. Accessed: Mar. 21, 2024. [Online]. Available: <https://www.johansondielectrics.com/downloads/ceramic-capacitoraging-made-simple.pdf>
- [9] R. Bosshard, J. W. Kolar, and B. Wunsch, "Control method for Inductive Power Transfer with high partial-load efficiency and resonance tracking," in *2014 International Power Electronics Conference (IPEC-Hiroshima 2014 - ECCE ASIA)*, May 2014, pp. 2167–2174. doi: 10.1109/IPEC.2014.6869889.
- [10] W. Li, G. Wei, C. Cui, X. Zhang, and Q. Zhang, "A Double-Side Self-Tuning LCC/S System Using a Variable Switched Capacitor Based on Parameter Recognition," *IEEE Trans. Ind. Electron.*, vol. 68, no. 4, pp. 3069–3078, Apr. 2021, doi: 10.1109/TIE.2020.2978726.
- [11] P. Tan, H. He, and X. Gao, "A Frequency-Tracking Method Based on a SOGI-PLL for Wireless Power Transfer Systems to Assure Operation in the Resonant State," *J. Power Electron.*, vol. 16, no. 3, pp. 1056–1066, May 2016, doi: 10.6113/JPE.2016.16.3.1056.
- [12] X. Dai and Y. Sun, "An Accurate Frequency Tracking Method Based on Short Current Detection for Inductive Power Transfer System," *IEEE Trans. Ind. Electron.*, vol. 61, no. 2, pp. 776–783, Feb. 2014, doi: 10.1109/TIE.2013.2257149.
- [13] Z. Zheng, N. Wang, and S. Ahmed, "Adaptive Frequency Tracking Control with Fuzzy PI Compound Controller for Magnetically Coupled Resonant Wireless Power Transfer," *Int. J. Fuzzy Syst.*, vol. 23, no. 6, pp. 1890–1903, Sep. 2021, doi: 10.1007/s40815-020-00890-1.
- [14] Y. Sun, H. Zhang, A. P. Hu, C.-S. Tang, and L.-J. Xiang, "The Recognition and Control of Nonideal Soft-Switching Frequency for Wireless Power Transfer System Based on Waveform Identification," *IEEE Trans. Power Electron.*, vol. 32, no. 8, pp. 6617–6627, Aug. 2017, doi: 10.1109/TPEL.2016.2603531.
- [15] M. Saad, Y. Ju, S. Khan, H. Ali, A. Wadood, and S. B. Rhee, "An Improved Algorithm for AC Impedance Extraction," *J. Electr. Eng. Technol.*, vol. 15, no. 6, pp. 2437–2450, Nov. 2020, doi: 10.1007/s42835-020-00518-2.
- [16] L. Shi, P. Alou, J. A. Oliver, J. C. Rodriguez, A. Delgado, and J. A. Cobos, "A Self-Adaptive Wireless Power Transfer System to Cancel the Reactance," *IEEE Trans. Ind. Electron.*, vol. 68, no. 12, pp. 12141–12151, Dec. 2021, doi: 10.1109/TIE.2020.3044817.
- [17] K. Matsuura, D. Kobuchi, Y. Narusue, and H. Morikawa, "Communication-Less Receiver-Side Resonant Frequency Tuning Method for Magnetically Coupled Wireless Power Transfer Systems," in *2021 IEEE Radio and Wireless Symposium (RWS)*, San Diego, CA, USA: IEEE, Jan. 2021, pp. 108–111. doi: 10.1109/RWS50353.2021.9360356.
- [18] R. Dai, R. Mai, and W. Zhou, "A Pulse Density Modulation Based Receiver Reactance Identification Method for Wireless Power Transfer System," *IEEE Trans. Power Electron.*, vol. 37, no. 9, pp. 11394–11405, Sep. 2022, doi: 10.1109/TPEL.2022.3167265.
- [19] C. Rong and B. Zhang, "A Fractional-Order Wireless Power Transfer System With Misalignment and Detuning Tolerance," *IEEE Trans. Power Electron.*, vol. 38, no. 12, pp. 14884–14895, Dec. 2023, doi: 10.1109/TPEL.2023.3319366.
- [20] C. Han, B. Zhang, Z. Fang, D. Qiu, Y. Chen, and W. Xiao, "Dual-Side Independent Switched Capacitor Control for Wireless Power Transfer with Coplanar Coils," *Energies*, vol. 11, no. 6, Art. no. 6, Jun. 2018, doi: 10.3390/en11061472.
- [21] P. Tan, B. Song, W. Lei, H. Yin, and B. Zhang, "Decoupling Control of Double-Side Frequency Tuning for LCC/S WPT System," *IEEE Trans. Ind. Electron.*, vol. 70, no. 11, pp. 11163–11173, Nov. 2023, doi: 10.1109/TIE.2022.3224139.
- [22] J. Liu, G. Wang, G. Xu, J. Peng, and H. Jiang, "A Parameter Identification Approach With Primary-Side Measurement for DC–DC Wireless-Power-Transfer Converters With Different Resonant Tank Topologies," *IEEE Trans. Transp. Electrification*, vol. 7, no. 3, pp. 1219–1235, Sep. 2021, doi: 10.1109/TTE.2020.3048026.
- [23] Y. Yang, S.-C. Tan, and S. Y. R. Hui, "Front-End Parameter Monitoring Method Based on Two-Layer Adaptive Differential Evolution for SS-Compensated Wireless Power Transfer Systems," *IEEE Trans. Ind. Inform.*, vol. 15, no. 11, pp. 6101–6113, Nov. 2019, doi: 10.1109/TII.2019.2924926.

- [24] C. Liu, W. Han, Y. Hu, and B. Zhang, "Simultaneous Identification of Multiple Parameters in Wireless Power Transfer Systems Using Primary Variable Capacitors," *Appl. Sci.*, vol. 14, no. 2, Art. no. 2, Jan. 2024, doi: 10.3390/app14020793.
- [25] S. A. Sis and S. Bicakci, "A resonance frequency tracker and source frequency tuner for inductively coupled wireless power transfer systems," in *2016 46th European Microwave Conference (EuMC)*, London, United Kingdom: IEEE, Oct. 2016, pp. 751–754. doi: 10.1109/EuMC.2016.7824452.
- [26] D.-W. Seo and J.-H. Lee, "Frequency-Tuning Method Using the Reflection Coefficient in a Wireless Power Transfer System," *IEEE Microw. Wirel. Compon. Lett.*, vol. 27, no. 11, pp. 959–961, Nov. 2017, doi: 10.1109/LMWC.2017.2750023.
- [27] K. Song *et al.*, "An Impedance Decoupling-Based Tuning Scheme for Wireless Power Transfer System Under Dual-Side Capacitance Drift," *IEEE Trans. Power Electron.*, vol. 36, no. 7, pp. 7526–7536, Jul. 2021, doi: 10.1109/TPEL.2020.3043229.
- [28] K. Harada, W. J. Gu, and K. Murata, "Controlled resonant converters with switching frequency fixed," in *1987 IEEE Power Electronics Specialists Conference*, Jun. 1987, pp. 431–438. doi: 10.1109/PESC.1987.7077212.